

Symmetry and Coplanarity of Organic Molecules Affect their Packing and Photovoltaic Properties in Solution-Processed Solar Cells

Shang-Che Lan,[†] Putikam Raghunath,[‡] Yueh-Hsin Lu,[†] Yi-Chien Wang,[†] Shu-Wei Lin,[†] Chih-Ming Liu,[†] Jian-Ming Jiang,[†] Ming-Chang Lin,^{‡,§} and Kung-Hwa Wei^{*,†}

[†]Department of Materials Science and Engineering, National Chiao Tung University, 300 Hsinchu City, Taiwan

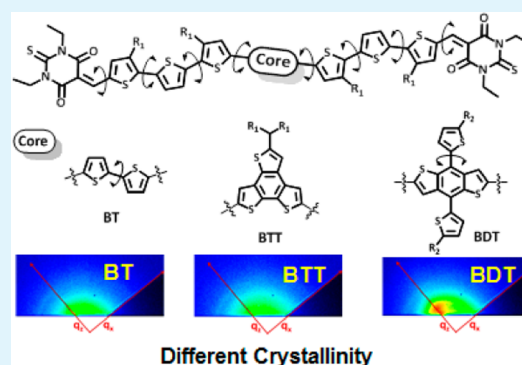
[‡]Center for Interdisciplinary Molecular Science, Department of Applied Chemistry, National Chiao Tung University, 300 Hsinchu City, Taiwan

[§]Department of Chemistry, Emory University, Atlanta, Georgia 30322, United States

Supporting Information

ABSTRACT: In this study we synthesized three acceptor–donor–acceptor (A–D–A) organic molecules, **TB3t-BT**, **TB3t-BTT**, and **TB3t-BDT**, comprising 2,2'-bithiophene (BT), benzo[1,2-b:3,4-b':5,6-d'']trithiophene (BTT), and benzo[1,2-b;4,5-b']dithiophene (BDT) units, respectively, as central cores (donors), terthiophene (3t) as π -conjugated spacers, and thiobarbituric acid (TB) units as acceptors. These molecules display different degrees of coplanarity as evidenced by the differences in dihedral angles calculated from density functional theory. By using differential scanning calorimetry and X-ray diffractions for probing their crystallization characteristics and molecular packing in active layers, we found that the symmetry and coplanarity of molecules would significantly affect the melting/crystallization behavior and the formation of crystalline domains in the blend film with fullerene, PC₆₁BM. **TB3t-BT** and **TB3t-BDT**, which each possess an inversion center and display high crystallinity in their pristine state, but they have different driving forces in crystallization, presumably because of different degrees of coplanarity. On the other hand, the asymmetrical **TB3t-BTT** behaved as an amorphous material even though it possesses a coplanar structure. Among our tested systems, the device comprising as-spun **TB3t-BDT**/PC₆₁BM (6:4, w/w) active layer featured crystalline domains and displayed the highest power conversion efficiency (PCE) of 4.1%. In contrast, the as-spun **TB3t-BT**/PC₆₁BM (6:4, w/w) active layer showed well-mixed morphology and with a device PCE of 0.2%; it increased to 3.9% after annealing the active layer at 150 °C for 15 min. As for **TB3t-BTT**, it required a higher content of fullerene in the **TB3t-BTT**/PC₆₁BM (4:6, w/w) active layer to optimize its device PCE to 1.6%.

KEYWORDS: bulk heterojunctions, organic solar cell, solution-processed small molecules, crystallization



INTRODUCTION

Solution-processed organic photovoltaics (OPVs) prepared through roll-to-roll or inject printing and used within inexpensive, lightweight, flexible devices are being considered as next-generation energy sources.^{1–4} Among them, polymer/fullerene bulk heterojunction (BHJ) systems have been the most successful, having gained a great deal of attention over the past decade.⁵ Through the development of new molecular structures^{6,7} and modification of the methods for fabricating devices,^{8–10} the power conversion efficiencies (PCEs) of single¹¹ and tandem¹² cells have reached in excess of 9% and 10%, respectively.

The development of small molecules for BHJ solar cells has also attracted attention because they have several advantages over polymers, including well-defined structures, ready purification, and lower batch-to-batch variation. Most solution-processed devices incorporating small organic molecules, however, provide unsatisfactory fill factors (FF) and, therefore,

poor PCEs.^{13,14} Until recently, high-efficiency BHJ devices have been made primarily through the development of new molecules.^{15–17} The low FFs of BHJ devices incorporating small molecule/fullerene blends have resulted mainly from the amorphous nature of their films obtained after spin-coating.^{18–20} Charge transport in small molecules, as well as in semicrystalline conjugated polymers, are highly dependent on their molecular packing, except that conjugated polymers can also have charge transport in their chain directions.^{21–25} Therefore, controlling a small molecule's crystalline nature and its miscibility with fullerenes are both important aspects for improving the PCEs of corresponding devices. The packing of a small molecule can be very sensitive to its structure; therefore, it can have a large impact on a device's performance.^{26–28}

Received: March 20, 2014

Accepted: May 30, 2014

Published: May 30, 2014

The design of suitable solution-processable small molecules for organic photovoltaics is similar to that of conjugated polymeric systems. The first issue is optimizing its band gap and energy levels that determine the region over which it absorbs light; the second is optimizing its solubility. The use of a conjugated donor (D)–acceptor (A) structure is an effective means of lowering the band gap and tuning the energy levels.^{29,30} This approach has been adopted widely for the development of small organic molecules for OPVs, with many different D–A combinations^{31–33} and shapes.³⁴ The solubility of small molecules, similar to that of conjugated polymeric system, depends on the length and number of alkyl chains on the molecule.^{35,36} Moreover, the symmetry and molecular packing must be taken into account when interpreting the crystal morphology.

A molecule featuring an electron-donating central core, π -conjugated spacers, and electron-withdrawing end-caps could be suitable for the preparation of solution-processed OPVs. In such systems displaying promising OPV performances, cyanoacetate, and rhodamine acceptors have been employed in conjunction with various cores, including benzodithiophene,^{37,38} dithienosiole,^{39,40} benzotrithiophene,⁴¹ and thiophene.^{42,43} In this study, we introduced a relatively new acceptor, thiobarbituric acid, to this system. Because thiobarbituric acid contains two amide groups and a thione group, we expected it to have high electron affinity and low-lying frontier orbitals, thereby decreasing optical band gaps and maintaining low energy levels. Here, we used three different cores based on thiobarbituric acid to synthesize solution-processable small molecules, which we then investigated for their structure–property relationships and photovoltaic properties.

RESULTS AND DISCUSSION

Synthesis of Small Molecules. Scheme 1 displays the synthetic route that we used to prepare the target molecules. The terthiophene carbaldehyde and core molecules were prepared using methods described in the literature.^{39,44,45} We employed a Stille reaction to couple the central cores to terthiophene carbaldehyde, resulting in CHO3t-core species, which can be readily purified through column chromatography using hexane and EtOAc as the eluent; and then the target small molecules were obtained by Knoevenagel condensations of the CHO3t-core species and thiobarbituric acid. At room temperature, all of the compounds were poorly dissolved in toluene, chlorobenzene, and dichloromethane; chloroform was the preferred solvent. As expected, conjugated molecules presenting longer or branched alkyl chains exhibited greater solubility; indeed, the solubility in chloroform followed the order TB3t-BTT > TB3t-BDT > TB3t-BT (Table 1).

Theoretical Simulation. To further understand the structures and energy levels of these molecules, we performed theoretical simulations of their molecular geometries, frontier orbitals and absorption wavelengths with the hybrid density functional theory (DFT) at the B3LYP/6-31G(d) level using Gaussian 09W. Table 2 summarizes the dihedral angles of their optimal geometries. Further simulation results are placed in Supporting Information. These results show that the BT unit has an additional rotational freedom along backbone and features a dihedral angle (φ_0); therefore, it implies BT is a less rigid moiety. Furthermore, we also calculated the average dihedral angle (excluding φ_4 and φ_4') to estimate the coplanarity of molecular backbone; the values are 8.53°,

Scheme 1. General Procedure for the Syntheses of TB3t-BT, TB3t-BTT, and TB3t-BDT

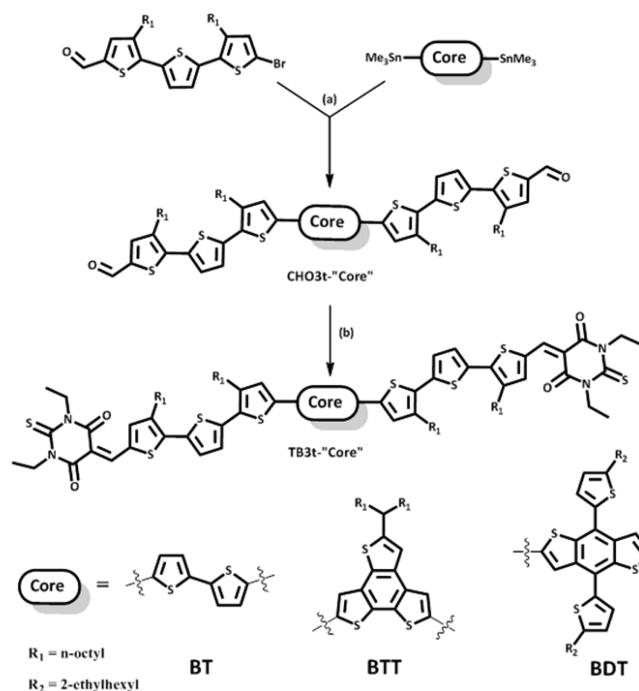


Table 1. Thermal Properties and Solubilities of the Three Small Molecules

material	thermal properties			solubility (mg mL ⁻¹) ^c
	T_d (°C) ^a	T_m (°C) ^b	T_c (°C) ^b	
TB3t-BT	348	227	174	6.3
TB3t-BTT	368	190, 204	173, 151, 144 ^d	14.5
TB3t-BDT	358	240	206	11.0

^aTemperature of 5% weight loss under N₂, determined through TGA.

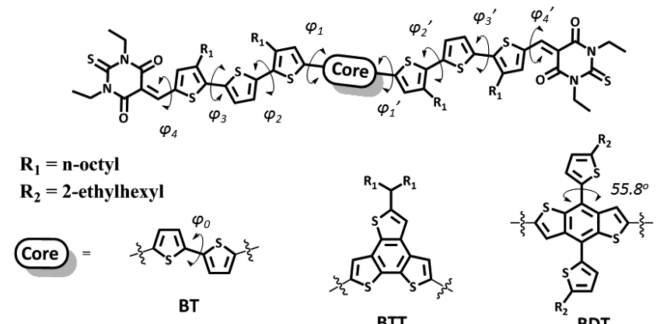
^bMelting and crystallization temperatures under N₂, determined through DSC. ^cSolubility in CHCl₃ at room temperature, determined following ASTM E1148. ^dCold crystallization.

5.95°, and 7.60° for TB3t-BT, TB3t-BTT, and TB3t-BDT, respectively. These results imply that TB3t-BT features the most twisted conformation among three molecules.

Using the optimized structures of TB3t-BT, TB3t-BTT and TB3t-BDT molecules with the B3LYP functional, the corresponding optical gaps have been calculated as listed in Supporting Information Table S1, together with the HOMO and LUMO energies. We have plotted the iso-surfaces (iso-value = 0.02) of the frontier molecular orbitals (FMOs) for all the molecules as shown in Supporting Information Figure S1. The results show that the molecular orbitals of HOMO and LUMO for all the three molecules are predominantly localized on the whole main chain. The molecular orbitals of the HOMO electronic densities are mainly located on the central part of the molecules, whereas the contribution to LUMO is mainly from the terminal group of TB.

The detailed analysis of these long wavelength absorptions (λ_{max}) as well as their main contributions to the first excitation can be made on the basis of time-dependent DFT (TDDFT) calculations as collected in Supporting Information Table S1. For the S₀ → S₁ transition, the calculated wavelengths for the TB3t-BT, TB3t-BTT, and TB3t-BDT molecules are 714, 697,

Table 2. Dihedral Angles of the Three Molecules from Theoretical Simulations



material	φ_4 (deg)	φ_3 (deg)	φ_2 (deg)	φ_1 (deg)	φ_0 (deg)	φ_1' (deg)	φ_2' (deg)	φ_3' (deg)	φ_4' (deg)
TB3t-BT	0.58	3.53	10.96	10.93	8.85	10.28	11.74	3.47	0.20
TB3t-BTT	2.17	11.57	4.91	0.64		1.05	7.00	10.54	1.47
TB3t-BDT	2.54	7.91	4.47	4.32		7.21	14.73	7.00	2.15

and 699 nm (excitation energy ΔE , 1.74, 1.78, and 1.77 eV) with oscillator strengths of 3.418, 2.969 and 3.110, respectively, resulting mainly from the HOMO \rightarrow LUMO transition.

Thermal Properties. We used TGA to determine the thermal stability of our synthesized organic compounds. Supporting Information Figure S2 displays the TGA curves recorded at a heating rate of 10 $^{\circ}\text{C min}^{-1}$ under N_2 . All compounds began to decompose when the temperature was higher than 300 $^{\circ}\text{C}$; each 5% weight loss temperature (T_d) was approximately 350 $^{\circ}\text{C}$, which is suitable for the application in optoelectronic devices.

Figure 1 displays the thermal phase transitions, including melting temperatures (T_m) and crystallization temperatures

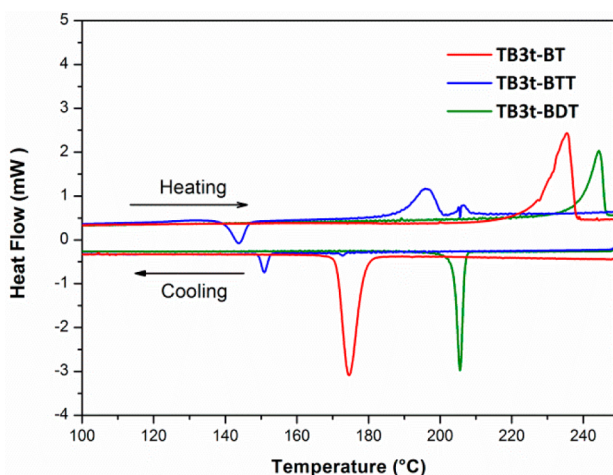


Figure 1. DSC curves of TB3t-BT, TB3t-BTT, and TB3t-BDT. Heating and cooling rates: 5 $^{\circ}\text{C min}^{-1}$.

(T_c), of our compounds, as characterized using DSC; Table 1 lists these values. The values of T_m and T_c both followed the same sequence: TB3t-BDT > TB3t-BT > TB3t-BTT. In previous studies of similar chemical structures, compounds displaying poorer solubility have often exhibited stronger molecular interactions and, thus, higher values of T_m .^{26,27} We found, however, that TB3t-BDT with its intermediate solubility, and not the most-insoluble TB3t-BT, provided the highest value of T_m , indicating that there is another factor that affected the melting temperature in our case. Indeed, the melting temperature of an organic crystal is affected by several

factors, including the molecular symmetry (packing), interaction energies and entropy, etc.⁴⁶ For our compounds, TB3t-BT and TB3t-BDT, which each possess an inversion center, are more symmetrical than TB3t-BTT; therefore, the former pair display higher melting temperatures and stronger crystallization relative to the latter, because of more ordered stacking in the solid state. Notably, TB3t-BTT displayed a cold crystallization peak at 144 $^{\circ}\text{C}$ upon heating, implying that it has significant amorphous characteristics which dues to its asymmetrical core. On the other hand, we also found that TB3t-BDT has higher tendency to crystallize than TB3t-BT, as indicated by the temperature difference (ΔT) between their T_m and T_c . ($\Delta T = 34$ and 53 $^{\circ}\text{C}$ for TB3t-BDT and TB3t-BT, respectively.) We suspect the fact that TB3t-BDT has higher T_m and more tendency to crystallize than TB3t-BT is because TB3t-BDT features more planar conformation in the solid state.

XRD Patterns. We prepared samples for XRD analyses by drop-casting solutions of the molecules onto silicon wafer substrates and then subjecting the systems to thermal annealing at 150 $^{\circ}\text{C}$ for 15 min. Figure 2 reveals that all three compounds exhibited strong signals in the low-angle regions of their diffraction patterns (the signal peak at 2.7 $^{\circ}$ arose from the incident angle of the X-rays). The XRD pattern of TB3t-BTT featured a relatively sharp peak at 4.1 $^{\circ}$ with a d -spacing of 21.3 \AA ; in contrast, those of TB3t-BT and TB3t-BDT both exhibited broadened and split peaks that might comprise two subpeaks with similar d -spacings (23.8 and 21.3 \AA for TB3t-BT; 22.6 and 21.3 \AA for TB3t-BDT). Because the bulk single crystal structures of such compounds are often unknown, assignments of these features usually follow those of polymeric systems. However, the length perpendicular to the backbone (100) is similar to the half-length of the backbone (002) for all compounds based on molecular models; the assignment of these peaks is difficult because of the insufficient information from the XRD analyses. Nevertheless, the XRD patterns of TB3t-BT and TB3t-BDT suggested that their crystal structure have higher order of packing than that of TB3t-BTT, implying that the TB3t-BTT features some amorphous characteristic, which agreed with the DSC analysis results.

Optical Absorption Spectra and Electrochemical Analysis. Figure 3 displays normalized UV-vis absorption spectra of our synthesized molecules in dilute solutions, as well as in the form of thin films; Table 3 summarizes the peak positions and band gaps. Figure 3a reveals that all materials

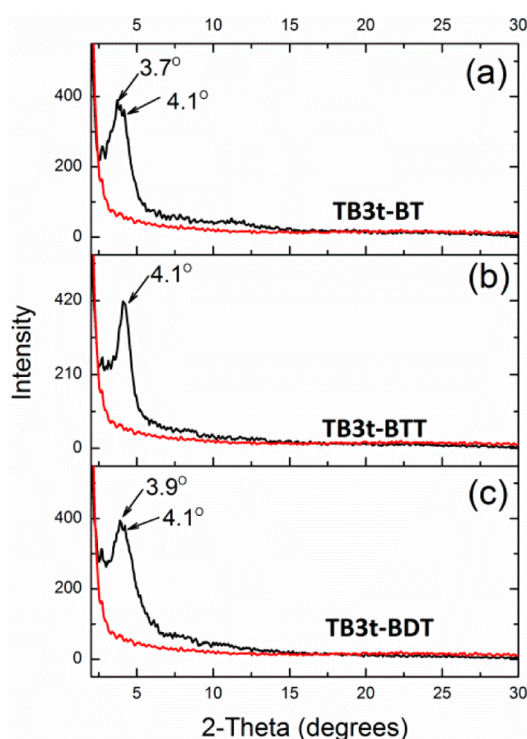


Figure 2. XRD pattern of (a) TB3t-BT, (b) TB3t-BTT, and (c) TB3t-BDT films drop-cast onto a silicon wafer substrate.

provided nearly identical absorption profiles for their dilute solutions. However, the TB3t-BT should have a narrower bandgap since it has better electron-donating abilities than others. The unexpected result is caused presumably by thermal disturbance of BT unit, resulting reduces the planarity of molecular backbone and conjugation length. The peaks appearing at 450 nm represent the π - π^* transitions; the most pronounced peaks, located at 565 nm, were due to internal charge transfer (ICT) from the donor unit to the acceptor unit.

The absorption spectra of the thin films of TB3t-BT, TB3t-BTT, and TB3t-BDT display apparent broadening and bathochromic red-shifts of the bands, relative to those from their dilute solutions because of their aggregation in the solid

Table 3. Optical and Electrochemical Properties of the Three Small Molecules

material	solution ^a		film ^b		energy levels	
	λ_{\max} (nm)	λ_{\max} (nm)	λ_{onset} (nm)	$E_{\text{g}}^{\text{opt}}$ (eV) ^c	HOMO (eV) ^d	LUMO (eV) ^e
TB3t-BT	447, 565	620	781	1.59	-5.12	-3.53
TB3t-BTT	445, 565	604	751	1.64	-5.19	-3.57
TB3t-BDT	455, 565	600	751	1.65	-5.20	-3.55

^aDilute solution in CHCl_3 . ^bSpin-coated from CHCl_3 onto ITO/PEDOT substrates. ^cOptical bandgaps calculated from $E_{\text{g}}^{\text{opt}} = 1240 \div \lambda_{\text{onset}}$ the absorption spectrum. ^dHOMO energy levels determined from onsets of the CV curves: $\text{HOMO} = -(4.8 + E_{\text{onset}}^{\text{ox}})$ eV. ^eLUMO energy levels determined from $E_{\text{LUMO}} = E_{\text{HOMO}} + E_{\text{g}}^{\text{opt}}$.

state. As compared to the organic molecules incorporating cyanoacetate^{37,41,43} and rhodamine¹⁶ as acceptor units, our molecules incorporating thiobarbituric acid as acceptor units exhibit greater shifts (~ 50 nm) toward long wavelengths in the visible region. Our compounds feature very broad absorption windows, especially TB3t-BT, which has a full width at half-maximum (fwhm) of 260 nm for its peak. These observations suggest that thiobarbituric acid is a very effective electron-acceptor unit that can decrease the band gap of a conjugated molecule. Moreover, each compound exhibited different degrees of red-shifting, following the sequence TB3t-BT > TB3t-BTT \cong TB3t-BDT because of the difference in electron-donating abilities of cores was enhanced when the molecules adopt more planar conformation from the solution to the film. This result is agreed with our simulation.

Notably, only the spectrum of TB3t-BTT featured a vibronic peak because of ordered π - π stacking of its molecules in the solid state. Sometimes the lack of vibronic peak is caused by the compound was settled too quickly from solution, so the peak can be emerged by thermal annealing. Supporting Information Figure S3 presents the absorption spectra of as-cast and annealed films of our three small organic molecules; the absorption profile of TB3t-BDT was unchanged after annealing, while vibronic peaks appeared for the annealed films of TB3t-BT. The lack of a vibronic peak indicates that TB3t-BDT prefers to adopt an *H*-aggregation state in the solid

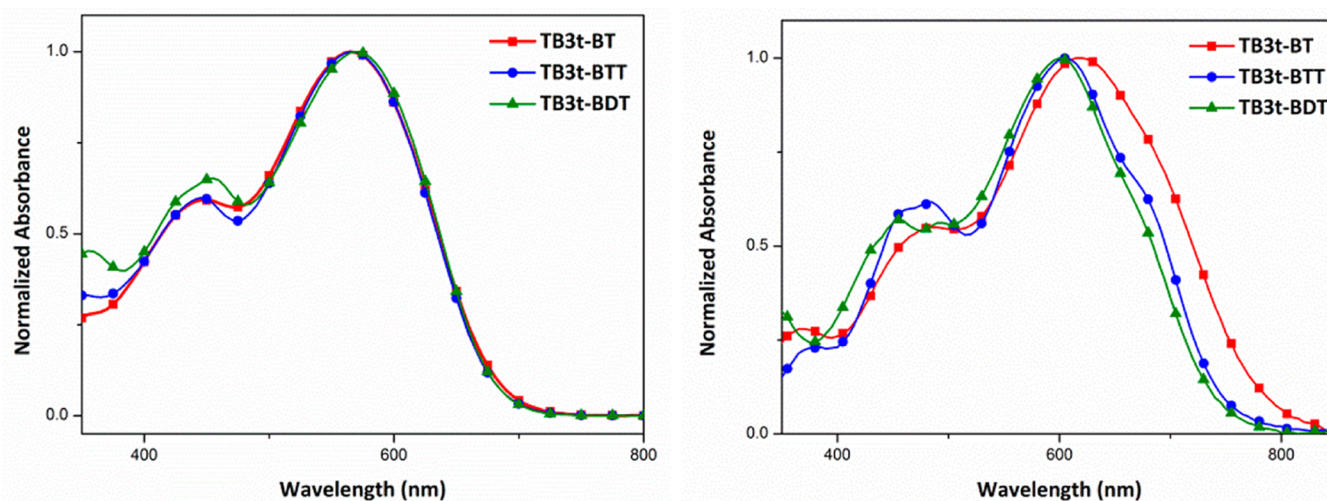


Figure 3. UV-vis absorption spectra of TB3t-BT, TB3t-BTT, and TB3t-BDT in the form of (a) solutions in CHCl_3 and (b) as-cast films.

state; in contrast, TB3t-BT and TB3t-BTT form *J*-aggregation states.

We used CV to determine the energy levels of the highest occupied molecular orbitals (HOMOs) of our three compounds; Table 3 lists the pertinent numerical data. All compounds exhibit low-lying HOMO energy levels, suggesting that photovoltaic devices incorporating them should exhibit relatively high open-circuit voltages (V_{oc}). For our three molecules not only featured low band gaps, but retained their low-lying HOMO energy levels. This behavior suggests that the narrowing of the band gaps was due to lowering of the energy levels of the lowest unoccupied molecular orbitals (LUMOs) of the molecules, confirming that thiobarbituric acid is a strong acceptor unit.

Photovoltaic Devices. We fabricated BHJ OPVs using our three small organic molecules as p-type materials and PC₆₁BM as the n-type material in devices having the configuration glass/ITO/PEDOT:PSS/active layer/Ca/Al. Figure 4 displays the *J*–

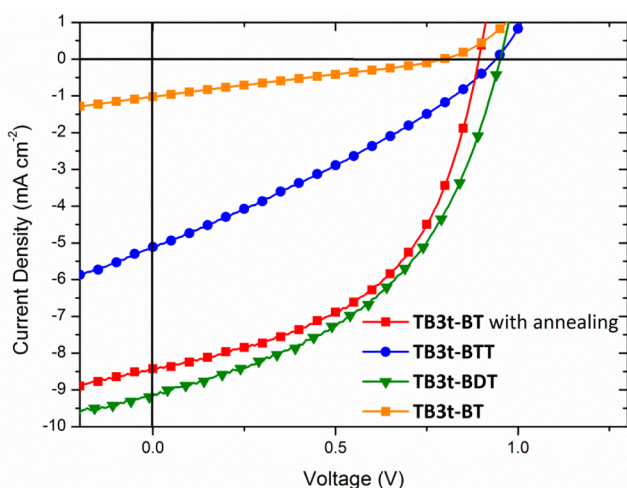


Figure 4. Current density–voltage curves of OPVs based on the organic molecules/PC₆₁BM under AM 1.5G illumination (100 mW cm⁻²).

Table 4. Characteristics of Photovoltaic Devices Incorporating Blends of Each Molecule with PC₆₁BM

material	ratio ^a	V_{oc} (V)	J_{sc} (mA cm ⁻²)	FF (%)	PCE (%)
TB3t-BT	6:4	0.77	0.94	27	0.2
	6:4 ^b	0.89	8.5	52	3.9
TB3t-BTT	4:6	0.93	5.3	32	1.6
TB3t-BDT	6:4	0.95	9.1	48	4.1

^aRatio of small molecule to PC₆₁BM. ^bAfter thermal treatment at 150 °C for 15 min.

V curves of these devices; Table 4 summarizes the photovoltaic parameters (see the Supporting Information for detailed curves and data). To determine the best composition for the devices, we tested various organic molecule–to–fullerene ratios for each compound, including weight ratios of 6/4, 5/5, and 4/6. All of these devices exhibited very high values of V_{oc} (>0.8 eV). The optimal device, obtained from an as-cast TB3t-BDT/PC₆₁BM blend film, exhibited a PCE of 4.1%, with a value of V_{oc} of 0.95 V, a value of J_{sc} of 9.1 mA cm⁻², and a FF of 48%. On contrast, annealing was critical for improving the

performance of the device based on TB3t-BT/PC₆₁BM; the PCE of the device prepared without thermal treatment was just 0.2%, whereas it enhanced dramatically to 3.9% after annealing. Both TB3t-BT and TB3t-BDT exhibited their best performance at a small molecule-to-fullerene ratio of 6/4, but TB3t-BTT required more PC₆₁BM (a ratio of 4/6) to optimize its PCE (1.6%). On the basis of our testes, all three molecules need quite different fabricated condition for their optimal devices. In conjugated polymeric systems, amorphous polymers are usually mixed with greater amounts of fullerenes to ensure optimal compositions for the active layers of devices. On the basis of our DSC analysis, TB3t-BTT possesses least driving force for crystallization among three molecules and possibly behaves as an amorphous material, which probably has better miscibility with fullerenes.

Morphological Analyses. Figure 5 displays tapping-mode AFM images of the surface morphologies of the active layers, as well as height and phase images, of the small molecule/PC₆₁BM blend films. The root-mean-square (RMS) roughnesses of our TB3t-BT/PC₆₁BM, TB3t-BTT/PC₆₁BM, and TB3t-BDT/PC₆₁BM pristine films were 0.92, 0.97, and 1.05 nm, respectively. The rather smooth surface of active layers implied the films have good quality and no large aggregation. Based on the phase images of these films, only TB3t-BDT/PC₆₁BM (Figure 5h) featured a certain degrees of aggregation which usually referred to a fine p-type/n-type interpenetrating network that is beneficial for charge separation and transport; in contrast, the films of TB3t-BT/PC₆₁BM and TB3t-BTT/PC₆₁BM showed homogeneous structures. This finding explained the reason for the device fabricated by as-spun TB3t-BDT/PC₆₁BM showed highest PCE. The annealed film of TB3t-BT/PC₆₁BM (Figure 5b) possessed a rougher surface (RMS = 4.9 nm) with some aggregation because of recrystallization of TB3t-BT. The annealing process ensured that TB3t-BT/PC₆₁BM formed a more favorable morphology, thereby resulting in a greater PCE for the corresponding device.

Because the packing of small molecules in a BHJ is a critical factor affecting the FF and PCE of a device, we used synchrotron grazing-incidence wide-angle X-ray scattering (GIWAXS) to quantitatively determine the molecular packing and orientation in our blend films. Figure 6 presents 2D images of the blend films; those of TB3t-BT and TB3t-BTT featured no apparent peaks, with only that of TB3t-BDT providing an evident, but featureless, scatter signal. This result implies that TB3t-BDT (Figure 6d) exhibited a fine crystalline structure in the active layer upon film formation. In contrast, the film of TB3t-BT/PC₆₁BM required thermal treatment, displaying a strong signal after annealing, to the recrystallization of TB3t-BT (Figure 6b). On the basis of the morphology analysis, the TB3t-BT and TB3t-BDT appear to have different miscibilities with PC₆₁BM, presumably because of the different driving forces for crystallization. TB3t-BDT has higher tendency to crystallize than TB3t-BT; therefore, it is easier to form crystalline domains in blend films as spin-casting.

CONCLUSIONS

We have synthesized three new conjugation molecules, TB3t-BT, TB3t-BTT, and TB3t-BDT, that feature bithiophene, benzotrithiophene, and benzodithiophene units, respectively, as their central cores, terthiophene units as π -conjugated spacers, and a new acceptor, thiobarbituric acid, as end-capping moieties. From theoretical simulations (DFT-B3LYP) on their optimal geometries, three molecules display different

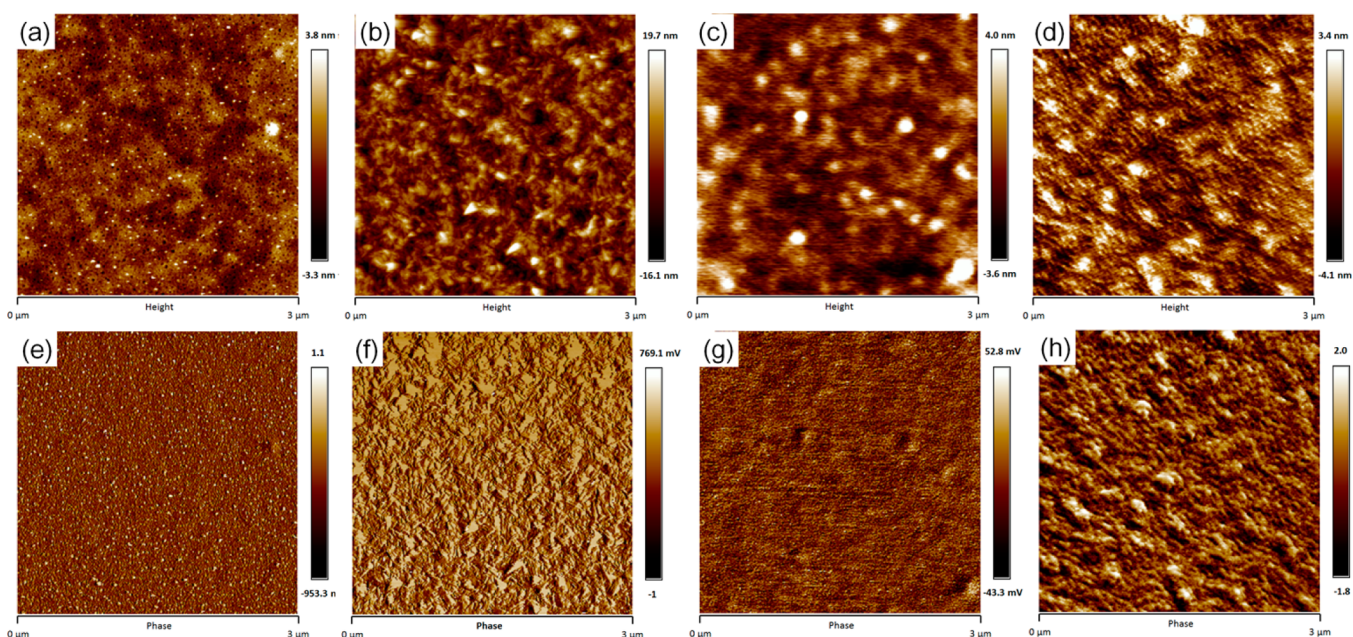


Figure 5. Tapping-mode AFM height (top) and phase (bottom) images ($3 \times 3 \mu\text{m}$) of blend films based on ratio of active. (a, e) Pristine film of TB3t-BT/PC₆₁BM. (b, f) Annealed film of TB3t-BT/PC₆₁BM. (c, g) Pristine film of TB3t-BTT/PC₆₁BM. (d, h) Pristine film of TB3t-BDT/PC₆₁BM.

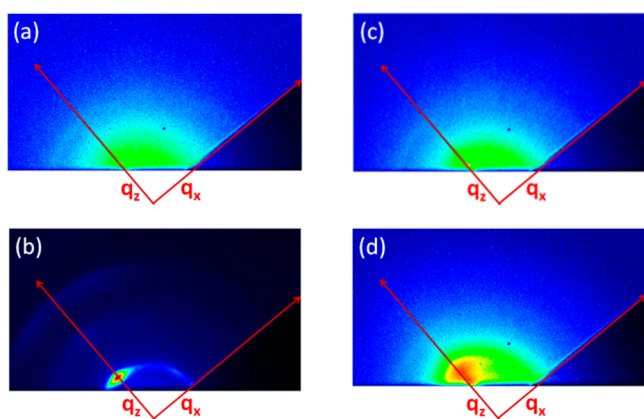


Figure 6. Two-dimensional GIWAXS images of blend films of (a) TB3t-BT:PC₆₁BM film as-cast, (b) TB3t-BT:PC₆₁BM film annealed at 150 °C, (c) TB3t-BTT:PC₆₁BM film as-cast, and (d) TB3t-BDT:PC₆₁BM film as-cast. All samples were on wafer/PEDOT: PSS substrates.

dihedral angles and thus different degrees of coplanarity. The absorption spectra of these three molecules cover the full visible spectrum (400–800 nm); in addition, they all occurred at low-lying energy levels, implying that thiobarbituric acid is a potentially useful electron acceptor when synthesizing low-band gap conjugated organic molecules for application in photo-voltaic devices exhibiting high open-circuit voltages.

The molecular structures of these cores significantly affected the melting and crystallization behaviors and the formation of crystalline domains in blend films with PC₆₁BM. TB3t-BT and TB3t-BDT, which have inversion centers and display high crystallinity, whereas TB3t-BTT is asymmetrical and has more amorphous characteristics. Furthermore, the coplanarity of TB3t-BT and TB3t-BDT affects their crystallization. The core of TB3t-BDT is more rigid than that of TB3t-BT, resulting in the former having a higher value of T_m and a greater tendency

to crystallize. An OPV device incorporating an as-cast TB3t-BDT/PC₆₁BM (6/4, w/w) blend film exhibited a PCE (4.1%) substantially higher than those of the other two because of a higher degrees of crystalline domains in its as-cast active layer. TB3t-BT forms a well-mixed morphology with PC₆₁BM at a ratio of 6/4; therefore, its devices required thermal annealing to increase the PCE from 0.2% to 3.9%. On the other hand, TB3t-BTT behaves much like an amorphous polymer, requiring a relatively high content of fullerene to achieve the optimal composition; indeed, the best ratio for devices prepared with TB3t-BTT/PC₆₁BM was 4/6, resulting in a PCE of 1.6%. We conclude that a more symmetrical and rigid core might provide such small molecules with a greater crystallinity and less miscibility with PC₆₁BM, factors that significantly influence the properties of their OPVs.

EXPERIMENTAL SECTION

Materials. Unless stated otherwise, all reactants and reagents were obtained commercially and used without further purification. The solvents were dried using appropriate agents and purged with N₂. All reactions and manipulations were performed under N₂. 5''-Bromo-3,3''-dioctyl-[2,2':5',2''-terthiophene]-5-carbaldehyde (Br3tCHO),³⁹ 2,6-bis(trimethylstannyl)-4,8-bis[5-(2-ethylhexyl)-thiophene-2-yl]-benzo[1,2-*b*;4,5-*b'*]dithiophene (BDT),⁴⁴ 5-(1-octylonyl)-2,8-bis(trimethylstannyl)benzo[1,2-*b*:3,4-*b'*:5,6-*d''*]trithiophene(BTT),⁴⁵ and 5,5'-bis(trimethylstannyl)-2,2'-bithiophene (BT) were synthesized according to literature procedures.

General Procedure for Stille Coupling CHO3t-core. A two-necked flask containing Br3tCHO (0.22 mmol), a stannyl compound (0.1 mmol), and anhydrous toluene (3 mL) was purged with N₂ for 20 min to remove O₂. In another flask, tris(dibenzylideneacetone)-dipalladium [Pd₂(dba)₃, 5 mg] and tri-*o*-tolylphosphine [P(*o*-tol)₃, 6.7 mg] were dissolved in toluene (5 mL) and then the solution was purged with N₂ for 20 min. An aliquot (2 mL) of the catalyst solution was injected into the first flask and then the mixture was heated at 100 °C for 24 h. After it was cooled to room temperature, the solvent was evaporated under vacuum. The residue was purified through column chromatography (SiO₂; EtOAc/hexane, 1:9) to give a red solid. A

small amount of CH_2Cl_2 was used to redissolve the solid, which was reprecipitated from MeOH to obtain the final compound.

CHO3t-BT. Yield: 75%. ^1H NMR (300 MHz, CDCl_3): δ (ppm) 9.81 (s, 2H), 7.58 (s, 2H), 7.23 (d, $J = 3.6$ Hz, 2H), 7.10 (d, $J = 3.9$ Hz, 2H), 7.07 (s, 4H), 7.01 (s, 2H), 2.84–2.73 (m, 8H), 1.66 (br, 8H), 1.40–1.23 (m, 45H), 0.86 (t, $J = 5.7$ Hz, 12H). MS (MALDI-TOF): calcd for $\text{C}_{92}\text{H}_{118}\text{O}_2\text{S}_{10}$ $[\text{M}]^+$, m/z 1574.63; found, m/z 1575.70.

CHO3t-BTT. Yield: 80%. ^1H NMR (300 MHz, CDCl_3): δ (ppm) 9.81 (s, 2H), 7.61 (s, 1H), 7.57 (s, 2H), 7.47 (s, 1H), 7.34 (s, 1H), 7.15–7.11 (m, 4H), 3.01 (br, 1H), 2.82–2.76 (m, 8H), 1.80–1.69 (m, 12H), 1.50–1.21 (m, 64H), 0.87–0.80 (m, 18H). MS (MALDI-TOF): calcd for $\text{C}_{66}\text{H}_{82}\text{O}_2\text{S}_8$ $[\text{M}]^+$, m/z 1162.41; found, m/z 1162.34.

CHO3t-BDT. Yield: 56%. ^1H NMR (300 MHz, CDCl_3): δ (ppm) 9.83 (s, 2H), 7.64 (s, 2H), 7.60 (s, 2H), 7.32 (d, $J = 3.3$ Hz, 2H), 7.25 (d, 2H), 7.14 (s, 2H), 7.13 (d, $J = 3.9$ Hz, 2H), 6.94 (d, $J = 3.3$ Hz, 2H), 2.91–2.74 (m, 12H), 1.75–1.60 (m, 10H), 1.38–1.25 (m, 56H), 1.00–0.85 (m, 24H). MS (MALDI-TOF): calcd for $\text{C}_{97}\text{H}_{116}\text{O}_2\text{S}_9$ $[\text{M}]^+$, m/z 1480.65; found, m/z 1480.56.

General Procedure for Knoevenagel Condensation. The aldehyde (0.05 mmol) was dissolved in dry CHCl_3 (5 mL) under a flow of N_2 in a two-necked flask and then pyridine (0.2 mL) and 1,3-diethyl-2-thiobarbituric acid (0.5 mmol) were added. After it was stirred at room temperature for 12 h, the solvent was evaporated under reduced pressure. The residue was washed with hot EtOH and then subjected to chromatographic purification (SiO_2 ; CHCl_3 /hexane, 3:1). The isolated compound was recrystallized (toluene/isopropanol) to afford a dark solid.

TB3t-BT. Yield: 80%. ^1H NMR (300 MHz, CDCl_3): δ (ppm) 8.54 (s, 2H), 7.67 (s, 2H), 7.46 (d, $J = 3.9$ Hz, 2H), 7.14 (d, $J = 4.2$ Hz, 2H), 7.06 (s, 4H), 7.01 (s, 2H), 4.62–4.52 (m, 8H), 2.84 (t, $J = 7.5$ Hz, 4H), 2.77 (t, $J = 7.2$ Hz, 4H), 1.70–1.65 (m, 8H), 1.40–1.22 (m, 52H), 0.87–0.83 (m, 12H). MS (MALDI-TOF): calcd for $\text{C}_{82}\text{H}_{102}\text{N}_4\text{O}_4\text{S}_{10}$ $[\text{M}]^+$, m/z 1526.51; found, m/z 1526.36.

TB3t-BTT. Yield: 88%. ^1H NMR (300 MHz, CDCl_3): δ (ppm) 8.74 (s, 1H), 8.46 (s, 1H), 7.60 (s, 1H), 7.57 (s, 1H), 7.55 (s, 1H), 7.44 (s, 1H), 7.45 (d, $J = 7.5$ Hz, 1H), 7.40 (s, 1H), 7.35 (s, 1H), 7.13–7.11 (m, 2H), 7.08 (s, 2H), 4.60–4.52 (m, 8H), 3.01 (br, 1H), 2.82–2.76 (m, 8H), 1.80–1.62 (m, 12H), 1.42–1.23 (m, 76H), 0.88–0.81 (m, 18H). MS (MALDI-TOF): calcd for $\text{C}_{103}\text{H}_{136}\text{N}_4\text{O}_4\text{S}_{11}$ $[\text{M}]^+$, m/z 1844.75; found, m/z 1844.72.

TB3t-BDT. Yield: 73%. ^1H NMR (300 MHz, CDCl_3): δ (ppm) 8.52 (s, 2H), 7.65 (s, 2H), 7.58 (s, 2H), 7.45 (d, $J = 3.9$ Hz, 2H), 7.31 (d, $J = 3.3$ Hz, 2H), 7.13 (d, $J = 4.2$ Hz, 2H), 7.08 (s, 2H), 6.93 (d, $J = 3.3$ Hz, 2H), 4.60–4.49 (m, 8H), 2.89 (d, $J = 6.3$ Hz, 4H), 2.82 (t, $J = 7.5$ Hz, 4H), 2.75 (t, $J = 6.9$ Hz, 4H), 1.72–1.60 (m, 10H), 1.48–1.26 (m, 68H), 1.00–0.83 (m, 24H). MS (MALDI-TOF): calcd for $\text{C}_{108}\text{H}_{138}\text{N}_4\text{O}_4\text{S}_{12}$ $[\text{M}]^+$, m/z 1938.74; found, m/z 1938.48.

Measurements and Characterizations. ^1H Nuclear magnetic resonance (NMR) spectra were recorded using a Bruker DRX-300 NMR spectrometer. Chemical shifts are reported relative to the solvent signal. Mass spectra were determined through matrix-assisted laser desorption/ionization time-of-flight mass spectrometry (MALDI-TOF MS), recorded using a Bruker Autoflex III instrument. Thermogravimetric analysis (TGA) was performed using a TA Instruments Q500 apparatus operated at a heating rate of $10\text{ }^\circ\text{C min}^{-1}$ under a N_2 flow. Differential scanning calorimetry (DSC) was performed using a PerkinElmer Pyris 1 apparatus; approximately 2.5 mg of the sample was analyzed at a heating rate of $5\text{ }^\circ\text{C min}^{-1}$. UV–vis absorption spectra were recorded using a Hitachi U-4100 spectrophotometer. Solid films were spin-coated from CHCl_3 solutions onto indium tin oxide (ITO)-coated glass presenting a 20 nm-thick buffer layer of poly(3,4-ethylenedioxythiophene)–poly(styrenesulfonate) (PEDOT:PSS). Cyclic voltammetry (CV) was performed using a BAS 100 electrochemical analyzer and a conventional three-electrode configuration: a glassy carbon electrode as the working electrode, a Pt wire as the counter electrode, and Ag/AgNO_3 (0.01 M in MeCN) as the reference electrode. Tetrabutylammonium hexafluorophosphate (Bu_4NPF_6 , 0.1 M) in MeCN was used as the supporting electrolyte. The small molecules were drop-coated onto the work electrode and analyzed at a scan rate of 50 mV s^{-1} . The ferrocene/ferrocenium ion

(Fc/Fc⁺) pair was used as the internal standard, with the assumption that the energy level of Fc is 4.8 eV below vacuum. X-ray diffraction (XRD) patterns of the drop-cast compounds on silicon wafers were obtained using a Bruker D8 instrument. Atomic force microscopy (AFM) was performed using a Digital Nanoscope III atomic force microscope operated in the tapping mode under ambient conditions. The thickness of the active layer of the device was measured using a Veeco Dektak 150 surface profiler. Grazing incidence wide-angle X-ray spectroscopy (GIWAXS) experiments were performed at the National Synchrotron Radiation Research Center.

Quantum Chemical Calculations. Quantum chemical calculations of these synthesized molecules have been performed to give a deeper insight into the electronic structure, absorption properties and the nature of their optical transitions using the density functional theory (DFT), implemented in the Gaussian 09 program.⁴⁷ The geometries of all the TB3t-BT, TB3t-BTT, and TB3t-BDT molecules were optimized at the hybrid DFT-B3LYP^{48–50} level of theory using the 6-31G(d) basis set. The optimized geometries were then subjected to the time dependent-density functional theory (TDDFT)⁵¹ calculations at the B3LYP/6-31G(d) level in order to obtain the S0 → S1 higher excited state transition energies of up to 10 excited states and oscillator strengths.

Fabrication and Measurement of Devices. Prepatterned ITO-coated glass was cleaned with detergent, DI water, acetone, and isopropanol in an ultrasonication bath (10 min each step) and then it was exposed to UV/ozone for 20 min prior to use. A thin layer (~20 nm) of PEDOT:PSS (Baytron P VP Al 4083) was spin-coated (4000 rpm, 60 s) onto the ITO substrate and then baked at $150\text{ }^\circ\text{C}$ for 15 min in air. The active layer, prepared from a hot CHCl_3 solution (10 mg mL^{-1} , $50\text{ }^\circ\text{C}$) containing a small molecule and PC_{61}BM , was spin-cast onto the PEDOT:PSS layer in a glovebox filled with dried N_2 . Finally, a 15 nm-thick Ca layer and a 100 nm-thick Al layer, for use as the counter electrode, were thermally deposited under vacuum on top of the active layer. Each device featured four cells with an effective layer area of 0.04 cm^2 . Current density–voltage (J – V) curves of the photovoltaic devices were recorded using a Keithley 2400 source meter under simulated AM 1.5 G illumination at 100 mW cm^{-2} using a Xe lamp-based Newport 66902 150-W solar simulator as a solar simulator. A silica photodiode (Hamamatsu S1133) was employed as a standard to confirm the light intensity.

■ ASSOCIATED CONTENT

Supporting Information

Additional experimental data, including DFT simulation results, TGA curves, CV curves, UV–vis absorption spectrum of annealed films, other device parameters, and ^1H NMR spectra. This material is available free of charge via the Internet at <http://pubs.acs.org>.

■ AUTHOR INFORMATION

Corresponding Author

*E-mail: khwei@mail.nctu.edu.tw.

Notes

The authors declare no competing financial interest.

■ ACKNOWLEDGMENTS

The authors thank the National Science Council, Taiwan, for financial support (NSC-102-3113-P-009-002).

■ REFERENCES

- (1) Hains, A. W.; Liang, Z.; Woodhouse, M. a.; Gregg, B. a. Molecular Semiconductors in Organic Photovoltaic Cells. *Chem. Rev.* **2010**, *110*, 6689–6735.
- (2) Beaujuge, P. M.; Reynolds, J. R. Color Control in π -Conjugated Organic Polymers for Use in Electrochromic Devices. *Chem. Rev.* **2010**, *110*, 268–320.

- (3) Salvatierra, R. V.; Cava, C. E.; Roman, L. S.; Zarbin, A. J. G. ITO-Free and Flexible Organic Photovoltaic Device Based on High Transparent and Conductive Polyaniline/Carbon Nanotube Thin Films. *Adv. Funct. Mater.* **2013**, *23*, 1490–1499.
- (4) Alstrup, J.; Jørgensen, M.; Medford, A.; Krebs, F. Ultra Fast and Parsimonious Materials Screening for Polymer Solar Cells Using Differentially Pumped Slot-Die Coating. *ACS Appl. Mater. Interfaces* **2010**, *2*, 2819–2827.
- (5) Su, Y.-W.; Lan, S.-C.; Wei, K.-H. Organic Photovoltaics. *Mater. Today* **2012**, *15*, 554–562.
- (6) Chen, H.-Y.; Hou, J.; Zhang, S.; Liang, Y.; Yang, G.; Yang, Y.; Yu, L.; Wu, Y.; Li, G. Polymer Solar Cells with Enhanced Open-Circuit Voltage and Efficiency. *Nat. Photonics* **2009**, *3*, 649–653.
- (7) Yuan, M.-C.; Chiu, M.-Y.; Liu, S.-P.; Chen, C.-M.; Wei, K.-H. A Thieno[3,4-*c*]pyrrole-4,6-Dione-Based Donor–Acceptor Polymer Exhibiting High Crystallinity for Photovoltaic Applications. *Macromolecules* **2010**, *43*, 6936–6938.
- (8) Wang, D. H.; Seifert, J.; Park, J. H.; Choi, D.-G.; Heeger, A. J. Efficiency Increase in Flexible Bulk Heterojunction Solar Cells with a Nano-Patterned Indium Zinc Oxide Anode. *Adv. Energy Mater.* **2012**, *2*, 1319–1322.
- (9) Chen, S.; Small, C. E.; Amb, C. M.; Subbiah, J.; Lai, T.; Tsang, S.-W.; Manders, J. R.; Reynolds, J. R.; So, F. Inverted Polymer Solar Cells with Reduced Interface Recombination. *Adv. Energy Mater.* **2012**, *2*, 1333–1337.
- (10) Wang, H.-S.; Chen, S.-Y.; Su, M.-H.; Wang, Y.-L.; Wei, K.-H. Inverted Heterojunction Solar Cells Incorporating Fullerene/Polythiophene Composite Core/Shell Nanorod Arrays. *Nanotechnology* **2010**, *21*, 145203–145211.
- (11) Liu, S.; Zhang, K.; Lu, J.; Zhang, J.; Yip, H.-L.; Huang, F.; Cao, Y. High-Efficiency Polymer Solar Cells via the Incorporation of an Amino-Functionalized Conjugated Metallopolymer as a Cathode Interlayer. *J. Am. Chem. Soc.* **2013**, *135*, 15326–15329.
- (12) You, J.; Dou, L.; Yoshimura, K.; Kato, T.; Ohya, K.; Moriarty, T.; Emery, K.; Chen, C.-C.; Gao, J.; Li, G.; Yang, Y. A Polymer Tandem Solar Cell with 10.6% Power Conversion Efficiency. *Nat. Commun.* **2013**, *4*, 1446–1455.
- (13) Takemoto, K.; Karasawa, M.; Kimura, M. Solution-Processed Bulk-Heterojunction Solar Cells Containing Self-Organized Disk-Shaped Donors. *ACS Appl. Mater. Interfaces* **2012**, *4*, 6289–6294.
- (14) Sahu, D.; Tsai, C.-H.; Wei, H.-Y.; Ho, K.-C.; Chang, F.-C.; Chu, C.-W. Synthesis and Applications of Novel Low Bandgap Star-Burst Molecules Containing a Triphenylamine Core and Dialkylated Diketopyrrolopyrrole Arms for Organic Photovoltaics. *J. Mater. Chem.* **2012**, *22*, 7945–7953.
- (15) Walker, B.; Tamayo, A. B.; Dang, X.-D.; Zalar, P.; Seo, J. H.; Garcia, A.; Tantiwivat, M.; Nguyen, T.-Q. Nanoscale Phase Separation and High Photovoltaic Efficiency in Solution-Processed, Small-Molecule Bulk Heterojunction Solar Cells. *Adv. Funct. Mater.* **2009**, *19*, 3063–3069.
- (16) Zhou, J.; Zuo, Y.; Wan, X.; Long, G.; Zhang, Q.; Ni, W.; Liu, Y.; Li, Z.; He, G.; Li, C.; Kan, B.; Li, M.; Chen, Y. Solution-Processed and High-Performance Organic Solar Cells Using Small Molecules with a Benzodithiophene Unit. *J. Am. Chem. Soc.* **2013**, *135*, 8484–8487.
- (17) Kyaw, A. K. K.; Wang, D. H.; Gupta, V.; Leong, W. L.; Ke, L.; Bazan, G. C.; Heeger, A. J. Intensity Dependence of Current–Voltage Characteristics and Recombination in High-Efficiency Solution-Processed Small-Molecule Solar Cells. *ACS Nano* **2013**, *7*, 4569–4577.
- (18) Mishra, A.; Bäuerle, P. Small Molecule Organic Semiconductors on the Move: Promises for Future Solar Energy Technology. *Angew. Chem., Int. Ed. Engl.* **2012**, *51*, 2020–2067.
- (19) Walker, B.; Kim, C.; Nguyen, T.-Q. Small Molecule Solution-Processed Bulk Heterojunction Solar Cells. *Chem. Mater.* **2011**, *23*, 470–482.
- (20) Lin, Y.; Li, Y.; Zhan, X. Small Molecule Semiconductors for High-Efficiency Organic Photovoltaics. *Chem. Soc. Rev.* **2012**, *41*, 4245–4272.
- (21) Coropceanu, V.; Cornil, J.; da Silva Filho, D.; Olivier, Y.; Silbey, R.; Brédas, J.-L. Charge Transport in Organic Semiconductors. *Chem. Rev.* **2007**, *107*, 926–952.
- (22) Troisi, A. Charge Transport in High Mobility Molecular Semiconductors: Classical Models and New Theories. *Chem. Soc. Rev.* **2011**, *40*, 2347–2358.
- (23) Rivnay, J.; Steyrlleuthner, R.; Jimison, L. H.; Casadei, A.; Chen, Z.; Toney, M. F.; Facchetti, A.; Neher, D.; Salleo, A. Drastic Control of Texture in a High Performance N-Type Polymeric Semiconductor and Implications for Charge Transport. *Macromolecules* **2011**, *44*, 5246–5255.
- (24) Viterisi, A.; Gispert-Guirado, F.; Ryan, J. W.; Palomares, E. Formation of Highly Crystalline and Texturized Donor Domains in DPP(TBFu)2:PC71BM SM-BHJ Devices via Solvent Vapour Annealing: Implications for Device Function. *J. Mater. Chem.* **2012**, *22*, 15175–15182.
- (25) Chen, G.-Y.; Cheng, Y.-H.; Chou, Y.-J.; Su, M.-S.; Chen, C.-M.; Wei, K.-H. Crystalline Conjugated Polymer Containing Fused 2,5-Di(thiophen-2-yl)thieno[2,3-*B*]thiophene and thieno[3,4-*C*]pyrrole-4,6-Dione Units for Bulk Heterojunction Solar Cells. *Chem. Commun.* **2011**, *47*, 5064–5066.
- (26) Eisenmenger, N. D.; Su, G. M.; Welch, G. C.; Takacs, C. J.; Bazan, G. C.; Kramer, E. J.; Chabinyc, M. L. Effect of Bridging Atom Identity on the Morphological Behavior of Solution-Processed Small Molecule Bulk Heterojunction Photovoltaics. *Chem. Mater.* **2013**, *25*, 1688–1698.
- (27) Liu, J.; Walker, B.; Tamayo, A.; Zhang, Y.; Nguyen, T.-Q. Effects of Heteroatom Substitutions on the Crystal Structure, Film Formation, and Optoelectronic Properties of Diketopyrrolopyrrole-Based Materials. *Adv. Funct. Mater.* **2013**, *23*, 47–56.
- (28) Graham, K. R.; Stalder, R.; Wieruszewski, P. M.; Patel, D. G. D.; Salazar, D. H.; Reynolds, J. R. Tailor-Made Additives for Morphology Control in Molecular Bulk-Heterojunction Photovoltaics. *ACS Appl. Mater. Interfaces* **2013**, *5*, 63–71.
- (29) Li, K.-C.; Hsu, Y.-C.; Lin, J.-T.; Yang, C.-C.; Wei, K.-H.; Lin, H.-C. Soluble Narrow-Band-Gap Copolymers Containing Novel Cyclopentadithiophene Units for Organic Photovoltaic Cell Applications. *J. Polym. Sci., Part A: Polym. Chem.* **2009**, *47*, 2073–2092.
- (30) Yuan, M.-C.; Chiu, M.-Y.; Chiang, C.-M.; Wei, K.-H. Synthesis and Characterization of Pyrido[3,4-*b*]pyrazine-Based Low-Bandgap Copolymers for Bulk Heterojunction Solar Cells. *Macromolecules* **2010**, *43*, 6270–6277.
- (31) Huang, J.; Zhan, C.; Zhang, X.; Zhao, Y.; Lu, Z.; Jia, H.; Jiang, B.; Ye, J.; Zhang, S.; Tang, A.; Liu, Y.; Pei, Q.; Yao, J. Solution-Processed DPP-Based Small Molecule That Gives High Photovoltaic Efficiency with Judicious Device Optimization. *ACS Appl. Mater. Interfaces* **2013**, *5*, 2033–2039.
- (32) Sun, Y.; Welch, G.; Leong, W.; Takacs, C.; Bazan, G.; Heeger, A. Solution-Processed Small-Molecule Solar Cells with 6.7% Efficiency. *Nat. Mater.* **2012**, *11*, 44–48.
- (33) Sharma, G. D.; Mikroyannidis, J. A.; Kurchania, R.; Thomas, K. R. J. Organic Bulk Heterojunction Solar Cells Based on Solution Processable Small Molecules (A- π -A) Featuring 2-(4-Nitrophenyl) Acrylonitrile Acceptors and Phthalimide-Based π -Linkers. *J. Mater. Chem.* **2012**, *22*, 13986–13995.
- (34) Shin, J.; Kang, N.; Kim, K.; Lee, T.; Jin, J.-I.; Kim, M.; Lee, K.; Ju, B.; Hong, J.-M.; Choi, D. J-Aggregation Induced Low Bandgap Anthracene-Based Conjugated Molecule for Solution-Processed Solar Cells. *Chem. Commun.* **2012**, *48*, 8490–8492.
- (35) Jiang, J.-M.; Yang, P.-A.; Chen, H.-C.; Wei, K.-H. Synthesis, Characterization, and Photovoltaic Properties of a Low-Bandgap Copolymer Based on 2,1,3-Benzoxadiazole. *Chem. Commun.* **2011**, *47*, 8877–8879.
- (36) Li, W.; Kelchtermans, M.; Wienk, M. M.; Janssen, R. A. J. Effect of Structure on the Solubility and Photovoltaic Properties of Bis-Diketopyrrolopyrrole Molecules. *J. Mater. Chem. A* **2013**, *1*, 15150–15157.
- (37) Zhou, J.; Wan, X.; Liu, Y.; Zuo, Y.; Li, Z.; He, G.; Long, G.; Ni, W.; Li, C.; Su, X.; Chen, Y. Small Molecules Based on Benzo[1,2-

b:4,5-*b'*]dithiophene Unit for High-Performance Solution-Processed Organic Solar Cells. *J. Am. Chem. Soc.* **2012**, *134*, 16345–16351.

(38) Patra, D.; Huang, T.-Y.; Chiang, C.-C.; Maturana, R. O. V.; Pao, C.-W.; Ho, K.-C.; Wei, K.-H.; Chu, C.-W. 2-Alkyl-5-Thienyl-Substituted benzo[1,2-*b*:4,5-*b'*]dithiophene-Based Donor Molecules for Solution-Processed Organic Solar Cells. *ACS Appl. Mater. Interfaces* **2013**, *5*, 9494–9500.

(39) Zhou, J.; Wan, X.; Liu, Y.; Long, G.; Wang, F.; Li, Z.; Zuo, Y.; Li, C.; Chen, Y. A Planar Small Molecule with Dithienosilole Core for High Efficiency Solution-Processed Organic Photovoltaic Cells. *Chem. Mater.* **2011**, *23*, 4666–4668.

(40) Ye, D.; Li, X.; Yan, L.; Zhang, W.; Hu, Z.; Liang, Y.; Fang, J.; Wong, W.-Y.; Wang, X. Dithienosilole-Bridged Small Molecules with Different Alkyl Group Substituents for Organic Solar Cells Exhibiting High Open-Circuit Voltage. *J. Mater. Chem. A* **2013**, *1*, 7622–7629.

(41) Patra, D.; Chiang, C.-C.; Chen, W.-A.; Wei, K.-H.; Wu, M.-C.; Chu, C.-W. Solution-Processed Benzotrithiophene-Based Donor Molecules for Efficient Bulk Heterojunction Solar Cells. *J. Mater. Chem. A* **2013**, *1*, 7767–7774.

(42) Liu, Y.; Wan, X.; Wang, F.; Zhou, J.; Long, G.; Tian, J.; You, J.; Yang, Y.; Chen, Y. Spin-Coated Small Molecules for High Performance Solar Cells. *Adv. Energy Mater.* **2011**, *1*, 771–775.

(43) Liu, Y.; Yang, Y.; Chen, C.-C.; Chen, Q.; Dou, L.; Hong, Z.; Li, G. Solution-Processed Small Molecules Using Different Electron Linkers for High-Performance Solar Cells. *Adv. Mater.* **2013**, *25*, 4657–4662.

(44) Huo, L.; Zhang, S.; Guo, X.; Xu, F.; Li, Y.; Hou, J. Replacing Alkoxy Groups with Alkylthienyl Groups: A Feasible Approach to Improve the Properties of Photovoltaic Polymers. *Angew. Chem., Int. Ed. Engl.* **2011**, *50*, 9697–9702.

(45) Lan, S.-C.; Yang, P.-A.; Zhu, M.-J.; Yu, C.-M.; Jiang, J.-M.; Wei, K.-H. Thiophene Spacers Impart Crystallinity and Enhance the Efficiency of Benzotrithiophene-Based Conjugated Polymers for Bulk Heterojunction Photovoltaics. *Polym. Chem.* **2013**, *4*, 1132–1140.

(46) Gavezzotti, A. Molecular Symmetry, Melting Temperatures and Melting Enthalpies of Substituted Benzenes and Naphthalenes. *J. Chem. Soc. Perkin Trans. 2* **1995**, 1399–1404.

(47) Frisch, M. J.; Trucks, G. W.; Schlegel, H. B.; Scuseria, G. E.; Robb, M. A.; Cheeseman, J. R.; Scalmani, G.; Barone, V.; Mennucci, B.; Petersson, G. A.; Nakatsuji, H.; Caricato, M.; Li, X.; Hratchian, H. P.; Izmaylov, A. F.; Bloino, J.; Zheng, G.; Sonnenberg, J. L.; Hada, M.; Ehara, M.; Toyota, K.; Fukuda, R.; Hasegawa, J.; Ishida, M.; Nakajima, T.; Honda, Y.; Kitao, O.; Nakai, H.; Vreven, T.; Montgomery, J. A., Jr.; Peralta, J. E.; Ogliaro, F.; Bearpark, M.; Heyd, J. J.; Brothers, E.; Kudin, K. N.; Staroverov, V. N.; Kobayashi, R.; Normand, J.; Raghavachari, K.; Rendell, A.; Burant, J. C.; Iyengar, S. S.; Tomasi, J.; Cossi, M.; Rega, N.; Millam, J. M.; Klene, M.; Knox, J. E.; Cross, J. B.; Bakken, V.; Adamo, C.; Jaramillo, J.; Gomperts, R.; Stratmann, R. E.; Yazyev, O.; Austin, A. J.; Cammi, R.; Pomelli, C.; Ochterski, J. W.; Martin, R. L.; Morokuma, K.; Zakrzewski, V. G.; Voth, G. A.; Salvador, P.; Dannenberg, J. J.; Dapprich, S.; Daniels, A. D.; Farkas, O.; Foresman, J. B.; Ortiz, J. V.; Cioslowski, J.; Fox, D. J. *Gaussian 09*; Gaussian, Inc.: Wallingford, CT, 2010.

(48) Becke, A. D. Density-Functional Exchange-Energy Approximation with Correct Asymptotic Behavior. *Phys. Rev. A* **1988**, *38*, 3098–3100.

(49) Becke, A. D. Density-Functional Thermochemistry. III. The Role of Exact Exchange. *J. Chem. Phys.* **1993**, *98*, 5648.

(50) Lee, C.; Yang, W.; Parr, R. G. Development of the Colle–Salvetti Correlation-Energy Formula into a Functional of the Electron Density. *Phys. Rev. B* **1988**, *37*, 785–789.

(51) Bauernschmitt, R.; Ahlrichs, R. Treatment of Electronic Excitations within the Adiabatic Approximation of Time Dependent Density Functional Theory. *Chem. Phys. Lett.* **1996**, *256*, 454–464.